

Energetics of a solar flare and a coronal mass ejection generated by a hot channel eruption

QINGMIN ZHANG,^{1,2} WEILIN TENG,^{3,1} DONG LI,^{1,2} JUN DAI,¹ AND YANJIE ZHANG¹

¹Key Laboratory of Dark Matter and Space Astronomy, Purple Mountain Observatory, CAS, Nanjing 210023, People's Republic of China

²Yunnan Key Laboratory of Solar physics and Space Science, Kunming 650216, People's Republic of China

³Department of Astronomy and Space Science, University of Science and Technology of China, Hefei 230026, People's Republic of China

ABSTRACT

Hot channels (HCs) are prevalent in the solar corona and play a critical role in driving flares and coronal mass ejections (CMEs). In this paper, we estimate the energy contents of an X1.4 eruptive flare with a fast CME generated by a HC eruption on 2011 September 22. Originating from NOAA active region 11302, the HC is the most dramatic feature in 131 and 94 Å images observed by the Atmospheric Imaging Assembly (AIA) on board the Solar Dynamics Observatory (SDO). The flare is simultaneously observed by SDO/AIA, the Reuven Ramaty High-Energy Solar Spectroscopic Imager (RHESSI), and the Extreme-Ultraviolet Imager (EUVI) on board the behind Solar TERrestrial Relations Observatory (STEREO). The CME is simultaneously detected by the white-light coronagraphs of the Large Angle Spectroscopic Coronagraph (LASCO) on board SOHO and the COR1 coronagraph on board the behind STEREO. Using multiwavelength and multiview observations of the eruption, various energy components of the HC, flare, and CME are calculated. The thermal and kinetic energies of the HC are $(1.77 \pm 0.61) \times 10^{30}$ erg and $(2.90 \pm 0.79) \times 10^{30}$ erg, respectively. The peak thermal energy of the flare and total radiative loss of SXR-emitting plasma are $(1.63 \pm 0.04) \times 10^{31}$ erg and $(1.03 - 1.31) \times 10^{31}$ erg, respectively. The ratio between the thermal energies of HC and flare is 0.11 ± 0.03 , suggesting that thermal energy of the HC is not negligible. The kinetic and potential energies of the CME are $(3.43 \pm 0.94) \times 10^{31}$ erg and $(2.66 \pm 0.49) \times 10^{30}$ erg, yielding a total energy of $(3.69 \pm 0.98) \times 10^{31}$ erg for the CME. Continuous heating of the HC is required to balance the rapid cooling by heat conduction, which probably originate from intermittent magnetic reconnection at the flare current sheet. Our investigation may provide insight into the buildup, release, and conversion of energies in large-scale solar eruptions.

Keywords: Sun: flares — Sun: coronal mass ejections (CMEs)

1. INTRODUCTION

A magnetic flux rope (MFR) is composed of a group of twisted magnetic field lines wrapping around a common axis (see [Cheng et al. 2017](#); [Liu 2020](#), and references therein). The helical structure of a MFR naturally provides dips to support the dense materials in solar prominences ([van Ballegooijen & Martens 1989](#); [Okamoto et al. 2008](#); [Zhou et al. 2018](#); [Jenkins & Keppens 2021](#); [Liakh & Keppens 2023](#)). MFRs play a central role in driving large-scale solar eruptions, leading to flares and coronal mass ejections (CMEs; [Chen 2011](#)). MFRs are involved in many theoretical models of eruptions, such as the ideal kink instability ([Török & Kliem 2005](#)), flux emergence

model ([Chen & Shibata 2000](#)), catastrophic loss of equilibrium model ([Lin & Forbes 2000](#)), tether-cutting model ([Moore et al. 2001](#); [Jiang et al. 2021](#)), and breakout model ([Lynch et al. 2004](#)). On the solar disk, MFRs may appear as sigmoids with a forward-S shape ([Aulanier et al. 2010](#); [Green et al. 2011](#); [Savcheva et al. 2012](#); [James et al. 2017](#)) or an inverse-S shape ([Rust & Kumar 1996](#); [Liu et al. 2010a](#); [Savcheva et al. 2016](#)). Above the solar limb, MFRs show up in extreme ultraviolet (EUV) and white light (WL) wavelengths ([Dere et al. 1999](#); [Yan et al. 2018](#); [Zhang et al. 2022a](#)). Occasionally, multiple MFRs are found to coexist in an active region (AR) and erupt sequentially ([Awasthi et al. 2018](#); [Hou et al. 2018](#); [Wang et al. 2018](#)). MFRs are mainly formed in the corona via magnetic reconnection between two J-shaped sheared arcades before or during eruptions ([van Ballegooijen & Martens 1989](#); [Amari et al. 2003](#); [Xia et al. 2014](#); [Xue et al. 2017](#)). Interaction between two sheared arcades is characterized by transient brightening

(Joshi et al. 2015) and bidirectional outflows (Cheng et al. 2015; Yan et al. 2021). The line-tied footpoints of MFRs may experience drifting motion due to continuous magnetic reconnection in the corona (Aulanier & Dudík 2019). Xing et al. (2020) proposed a new method and explored the evolution of toroidal flux of CME flux ropes during their eruptions. The toroidal flux of the CME flux rope rapidly increases before decreasing in a gradual way, which is similar to the evolution of SXR flux of the associated flare.

Hot channels (HCs) are bright structures first observed in 94 Å ($\log T[\text{K}] \approx 6.85$) and 131 Å ($\log T[\text{K}] \approx 7.05$) of the Atmospheric Imaging Assembly (AIA; Lemen et al. 2012) on board the Solar Dynamics Observatory (SDO) spacecraft (Cheng et al. 2011; Zhang et al. 2012). Due to the extraordinarily high temperatures, HCs are hardly visible in other EUV passbands of AIA (Cheng et al. 2012; Zhang et al. 2022b). Composite images show that HCs are surrounded by cooler leading edges or compression fronts observed in 171, 193, and 211 Å during eruptions. Apart from hot EUV and SXR passbands, HCs could be detected in microwaves (Wu et al. 2016). It is widely accepted that the magnetic configurations of HCs are MFRs, and HCs play a key role in generating CMEs (Cheng et al. 2013a; Nindos et al. 2015). HCs could be created before (Cheng et al. 2013a; Zhang et al. 2022b) or during eruptions (Cheng et al. 2011; Song et al. 2014; Chen et al. 2019; Gou et al. 2022). Statistical investigation reveals that $\sim 2/3$ and $\sim 1/3$ of them are formed before and during eruptions (Nindos et al. 2020), respectively.

Although HCs have drawn great attention in the past decade, the energetics of HCs is rarely explored. Using the differential emission measure (DEM) analysis (Hannah & Kontar 2012), Hannah & Kontar (2013) studied the erupting plasmoid on 2010 November 3 and calculated its temperature and density. After dividing the plasmoid into a core, an envelope, and a long stem (current sheet), they calculated thermal energy ($\sim 2.6 \times 10^{30}$ erg) and kinetic energy ($\sim 1.6 \times 10^{30}$ erg) of the plasmoid, respectively. Hence, the total energy including the two components reaches $\sim 4.2 \times 10^{30}$ erg. Note that the plasmoid core with temperatures of 11–14 MK is considered as the edge-on representative of the HC (Cheng et al. 2011). Since the associated flare was occulted by the eastern limb, they did not calculate the flare energy. In this paper, using multiwavelength and multiview observations on 2011 September 22, we study the eruption of a HC, which generates an X1.4 class flare and a fast halo CME in AR 11302 (N11E80). The flare commences at $\sim 10:29$ UT, peaks at $\sim 11:04$ UT, and stops after 12:00 UT (Figure 1(a)). We will estimate different energy components of the flare, CME, and HC. The paper is organized as follows. We describe observations and data analysis in Section 2. The energy components are obtained in Section 3 and compared

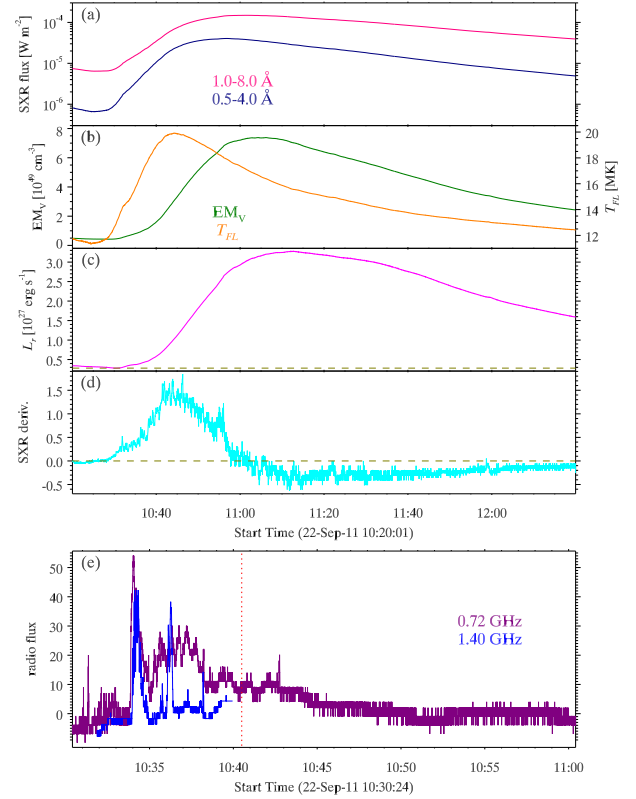


Figure 1. (a)–(d) Time evolutions of SXR fluxes in 1–8 Å (pink line) and 0.5–4 Å (dark blue line), volume emission measure (green line) and temperature (orange line), radiative loss rate of SXR-emitting plasma (magenta line), and SXR flux derivative (cyan line) of the X1.4 flare, respectively. (e) Time evolutions of the radio fluxes at 0.72 GHz (purple line) and 1.40 GHz (blue line) during the impulsive phase of the flare. The red dotted line denotes the time at 10:40:30 UT when v_{HC} reaches the linear speed of CME.

with previous results in Section 4. Finally, a brief conclusion is given in Section 5.

2. OBSERVATIONS AND DATA ANALYSIS

Figure 2(a)–(f) show six AIA 131 Å images during 10:20–11:04 UT (see also the animation). Panel (a) features the HC before eruption, which is pointed by the arrow. The HC lifts off slowly until $\sim 10:28$ UT (panel (b)). Afterwards, it starts to rise impulsively, generating the X1.4 flare below (panel (c)). The HC continues to ascend and expand laterally (panel (d)), leaving behind hot and bright post flare loops (PFLs) close to the flare peak time (panels (e)–(f)). The rising HC is also evident in 94 Å base-difference image in Figure 2(g). Figure 2(h) shows soft X-ray (SXR) image of the flare at 6–12 keV, which is obtained using the CLEAN method (Hurford et al. 2002) during 10:54:16–10:58:12 UT with the Reuven Ramaty High-Energy Solar Spectroscopic Imager (RHESSI; Lin et al. 2002). The integration time is 236 s and the detectors are 3F, 4F, 5F, 6F, 7F, and 8F. Since

emission at 6–12 keV is mainly from thermal electrons, the shape of the flare is very close to that in 131 Å (panel (e)).

In order to track the HC, a horizontal slice (S1) is selected along the direction of eruption in Figure 2(c). Time-distance diagrams of the slice in 131 and 94 Å are displayed in Figure 3. The evolution of the HC is similar in both passbands. In panel (a), the trajectory of the HC is marked with orange “+” symbols, which is characterized by a slow rise followed by a fast rise (Cheng et al. 2013b). In Figure 4(a), the same trajectory is marked with blue “+” symbols. To fit the trajectory, we use the equation (Cheng et al. 2013b):

$$h(t) = c_0 e^{t/\sigma} + c_1 t + c_2, \quad (1)$$

where t denotes time after t_0 (10:20:21 UT), $h(t)$ is height of the HC, and σ , c_0 , c_1 , and c_2 are free parameters. The onset time of fast rise is expressed as:

$$t_{\text{onset}} = \sigma \ln\left(\frac{c_1 \sigma}{c_0}\right). \quad (2)$$

In Figure 4, the time of t_{onset} at 10:27:48 UT (brown dotted line) is ~ 72 s earlier than the flare start time at 10:29:00 UT (orange dotted line), suggesting that the HC is formed before flare (Nindos et al. 2020). Evolution of the associated velocity ($v_{HC} = \frac{dh(t)}{dt}$) is displayed in Figure 4(b), showing that v_{HC} increases slowly from ~ 30 to ~ 50 km s $^{-1}$ at t_{onset} and increases impulsively to ~ 680 km s $^{-1}$ around 10:37 UT. Cheng et al. (2020) explored the early kinematic evolutions of 12 eruption events, including the HC eruption on 2011 September 22 (H3 in their list). Time-distance diagram of the HC in 131 Å is derived during 10:10–10:44 UT (see their Fig. 2(a)). Trajectory of the HC is extracted during 10:16–10:38 UT, which is fitted with various functions (see their Fig. 3(a)). The onset time of main acceleration obtained from Equation (1) is $\sim 10:25$ UT, which is ~ 3 minutes earlier than our result. There are two reasons for the inconsistency. Firstly, the trajectory of the HC is derived manually rather than automatically in both works. Hence, uncertainty of the HC leading edge is inevitable. Secondly, the start time of HC evolution is set to be 10:16:00 UT in Cheng et al. (2020), which is ~ 4 minutes earlier than that in our study (see Figure 4). Nevertheless, the inconsistency does not influence the calculation of the energetics of HC.

In Figure 5, the top and bottom panels show WL images of the related CME observed by C2 coronagraph of the Large Angle Spectroscopic Coronagraph (LASCO; Brueckner et al. 1995) on board SOHO¹ and by COR1 coronagraph on board the behind Solar TERrestrial Relations Observatory (STEREO; Kaiser et al. 2008), respectively. The behind STEREO (hereafter STB) has a separation angle of

96.5° with respect to the Sun-Earth connection on 2011 September 22. The CME first appears in the field of view (FOV) of LASCO/C2 at 10:48 UT and propagates eastward with a position angle of $\sim 71^\circ$. It is noted that the CME does not present a typical three-part structure (Song et al. 2023a,b; Zhou et al. 2023). Instead, it features a bright leading front without a trailing core. According to Equation (1), the HC rises to a height of ~ 410 Mm above the limb at 10:40:30 UT, which is still blocked by the occulting disk of LASCO/C2. The corresponding velocity (v_{HC}) increases to ~ 1909 km s $^{-1}$, which is close to the linear speed of CME. Assuming a constant speed after 10:40:30 UT, the HC should reach a height of $\sim 2.84 R_\odot$ at 10:48:06 UT, which is very close to the height of CME leading edge, i.e., $\sim 2.98 R_\odot$. In light of the direction and kinematics, it is most likely that the eruptive HC evolves into the CME leading edge (Vourlidas et al. 2013). The fast CME drives a shock wave indicated by the arrow in panel (c), which is accompanied by a type II radio burst (Zucca et al. 2014). In the FOV of STB/COR1, since the source region (AR 11302) is close to the disk center, the CME is full halo without a core.

Figure 6 shows radio dynamic spectra observed by e-Callisto/BLEN7M during 10:30–11:00 UT and Ondrejov/PHOENIX3 during 10:31–10:40 UT. The yellow arrows point to the type III radio bursts during 10:34–10:40 UT, with the frequency ranging from ~ 600 MHz to ~ 1600 MHz. The radio fluxes at 720 MHz and 1.40 GHz are extracted from the dynamic spectra and plotted in Figure 1(e). The radio spikes during 10:34–10:40 UT are roughly coincident with the spikes in GOES derivative flux in 1–8 Å as a proxy of HXR flux (Figure 1(d)). The occurrence of type III bursts is a signature of intermittent magnetic reconnection and particle acceleration during the flare impulsive phase (Kliem et al. 2000; Kou et al. 2022; Karlický 2023). In Figure 1(e), the red dotted line delineates the time (10:40:30 UT) when the HC speed gets close to the linear speed of CME, implying that acceleration of the HC may come to a halt when flare reconnection slows down.

In Figure 6(a), apart from the type III bursts, there is a moving type IV (type IVm) burst, whose frequency drifts from ~ 600 MHz to ~ 200 MHz during 10:40–10:56 UT. It is generally suggested that a type IVm burst results from emission of electrons trapped in an ascending MFR (Bain et al. 2014; Vasanth et al. 2019; Vemareddy et al. 2022). In our case, as the HC rises up, the electrons are trapped in it and produce type IVm burst.

3. ENERGETICS

To estimate thermal energy of the HC, we will first calculate its temperature using the DEM analysis (Cheng et al. 2012). Using simultaneous observations of six AIA passbands (94, 131, 171, 193, 211, and 335 Å), this method

¹ https://cdaw.gsfc.nasa.gov/CME_list/

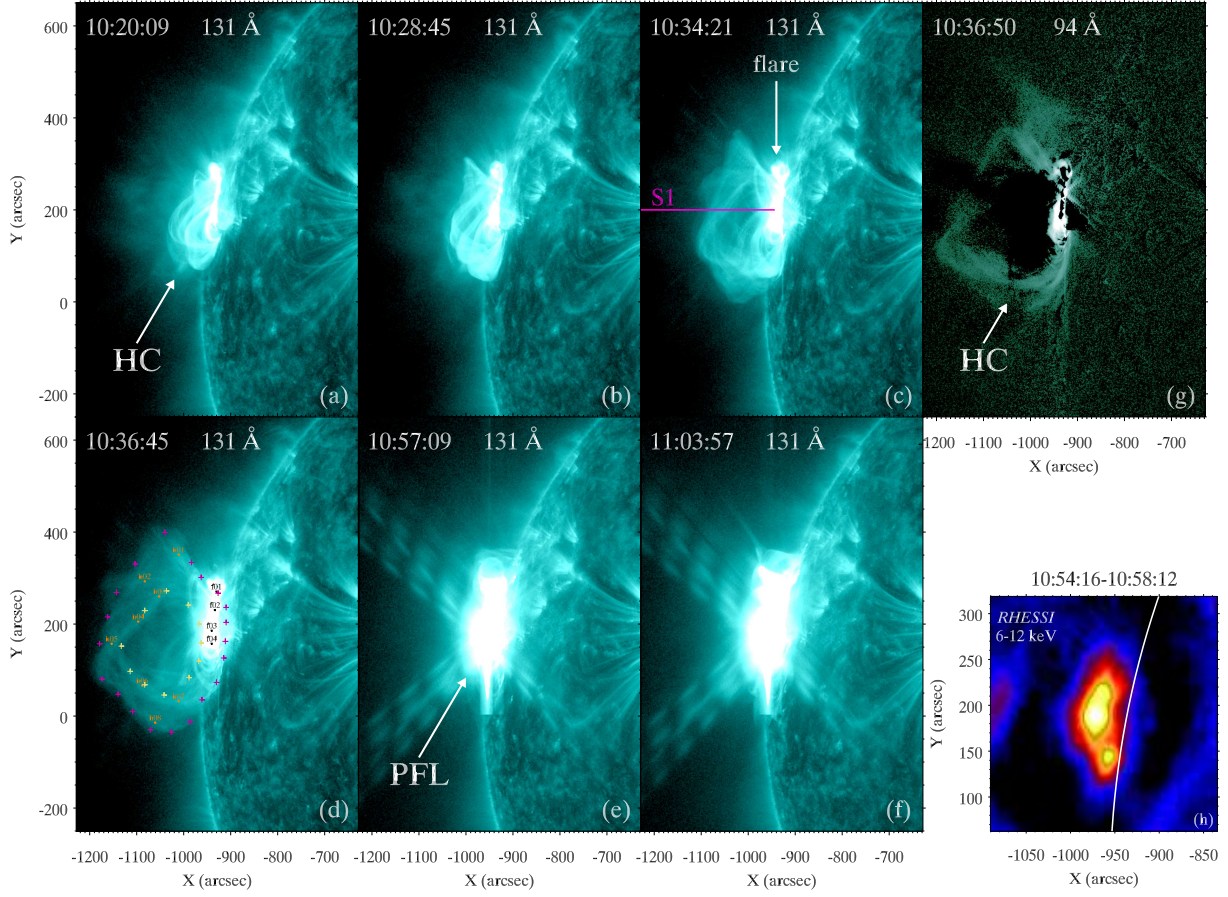


Figure 2. (a)–(f): AIA 131 Å images to illustrate the evolution of HC and flare. In panel (c), a horizontal slice (S1) with a length of 206.6 Mm is used to investigate the evolution of HC. In panel (d), the magenta and yellow “+” symbols represent the outer and inner boundaries of the HC and flare. Eight orange boxes (h01–h08) and four black boxes (f01–f04) are used to perform DEM analysis for the HC and flare, respectively. (g) AIA base-difference image in 94 Å at 10:36:50 UT. (h) SXR image of the flare at 6–12 keV obtained with RHESSI during 10:54–10:58 UT. An animation showing the HC eruption in AIA 131 and 94 Å is available. It covers a duration of 44 minutes from 10:20 UT to 11:04 UT on 2011 September 22. The entire movie runs for ~3 s. (An animation of this figure is available.)

has been widely applied to temperature diagnostics of HCs (Cheng et al. 2014), flare current sheets (Xue et al. 2016), and coronal jets (Zhang & Ji 2014; Zhang et al. 2016). The observed intensity of each passband (I_j) is determined by the temperature response function $R_j(T)$ and DEM(T) of the coronal plasma along the line of sight (LOS):

$$I_j = \int_{T_1}^{T_2} \text{DEM}(T) \times R_j(T) dT, \quad (3)$$

where $\log T_1$ and $\log T_2$ stand for the minimum and maximum temperatures for the integral. Column emission measure (EM_c) along the LOS is:

$$\text{EM}_c = \int_{T_1}^{T_2} \text{DEM}(T) dT = \int_0^H n_e^2 dh, \quad (4)$$

where n_e and H denote the electron number density and LOS depth. Hence, the DEM-weighted average temperature is:

$$\langle T \rangle = \frac{\int_{T_1}^{T_2} \text{DEM} \times T \times dT}{\text{EM}_c}. \quad (5)$$

Besides, Monte Carlo (MC) simulations are conducted to evaluate the confidence of DEM reconstruction (Cheng et al. 2012). In Figure 2(d), we select eight regions (h01–h08) within the HC and four regions (f01–f04) within the flare site at 10:36:45 UT, which are marked with orange and black boxes. Reconstructed DEM profiles of the 12 regions are plotted in Figure 7, with the values of $\langle T \rangle$ and $\log \text{EM}_c$ being labeled. For the HC, there are large uncertainties of DEM profiles at temperatures of $\log T < 5.9$ and $\log T > 7.1$. Therefore, we set $\log T_1[\text{K}] = 5.9$ and $\log T_2[\text{K}] = 7.1$ to calculate $\langle T \rangle$ and EM_c . $\langle T \rangle$ lies in the range of 4.8–5.8 MK, with a mean value of 5.27 MK and a standard deviation of 0.41 MK. Hence, $\langle T \rangle = 5.27 \pm 0.41$ MK (see Table 1). EM_c has a mean value of $2.70 \times 10^{27} \text{ cm}^{-5}$ and a standard deviation of $1.30 \times 10^{27} \text{ cm}^{-5}$, respectively. For the flare region, the uncertainties of DEM profiles are small at temperatures of $5.5 \leq \log T \leq 7.5$. Therefore, we set $\log T_1[\text{K}] = 5.5$ and $\log T_2[\text{K}] = 7.5$. $\langle T \rangle$ lies in the range of 7.53–11.47 MK,

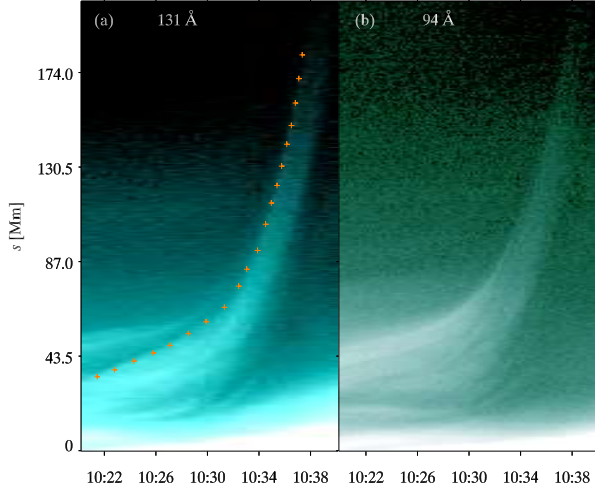


Figure 3. Time-distance diagrams of S1 in 131 and 94 Å. $s = 0$ and $s = 206.6$ Mm denote the west and east endpoints of S1, respectively.

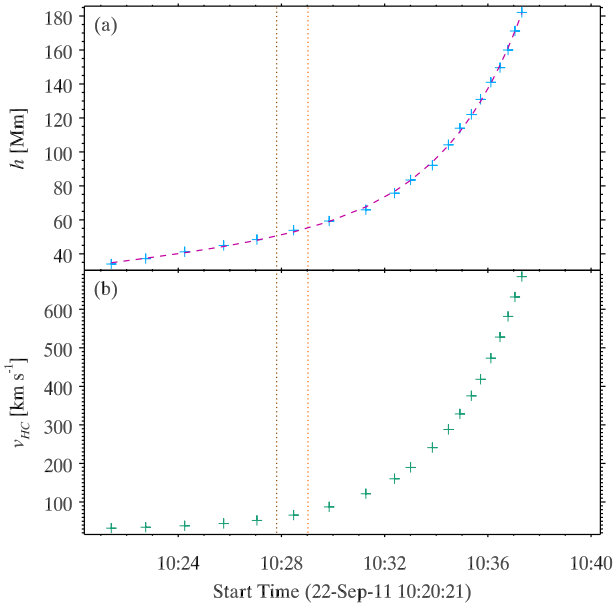


Figure 4. Time evolutions of the height (a) and velocity (b) of the HC. The pink dashed line delineates the result of curve fitting using Equation (1). The brown and orange dotted lines represent the onset time of fast rise and start time of the flare, respectively.

with a mean value of 9.51 MK. EM_c is nearly two orders of magnitude larger than that of HC. Note that the flare temperature recorded by GOES increases and reaches maximum at $\sim 10:44$ UT (Figure 1(b)).

The next step is to estimate the volume of the HC. We first attempt to fit the HC with the revised graduated cylindrical shell (GCS) model, which is proposed to reconstruct the 3D morphology of prominences or MFRs propagating non-

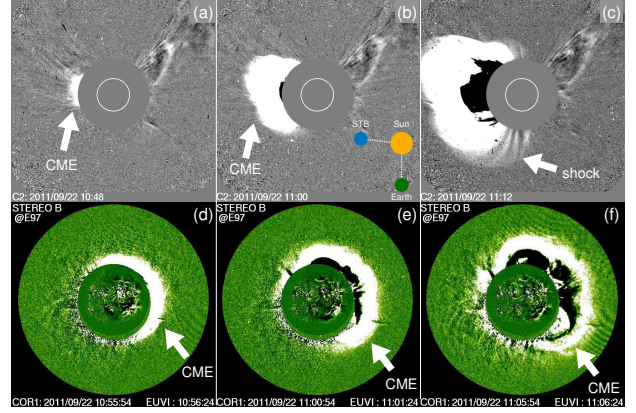


Figure 5. Running-difference images of the CME observed by LASCO/C2 during 10:48–11:12 UT (top panels) and STB/COR1 during 10:56–11:06 UT (bottom panels). The white arrows point to the CME and CME-driven shock.

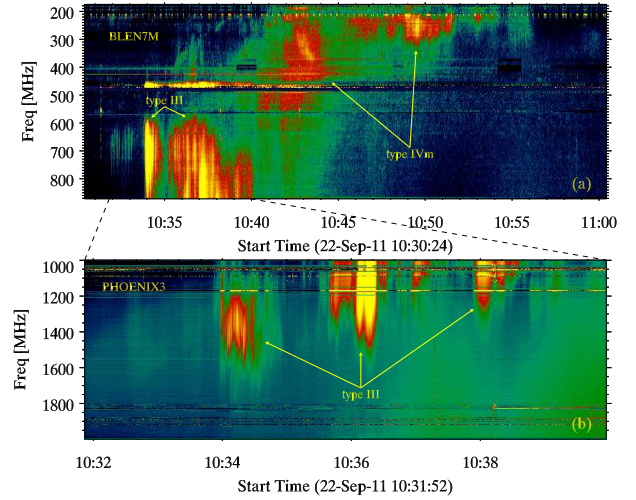


Figure 6. Radio dynamic spectra recorded by e-Callisto/BLEN7M (a) and Ondrejov/PHOENIX3 (b) during the flare impulsive phase. The yellow arrows point to the type III and IVm bursts.

Table 1. Temperature, volume, electron number density, and mass of the HC.

$\langle T \rangle$	V_{HC}	n_e	m_{HC}
(MK)	(cm^3)	(cm^{-3})	(g)
5.27 ± 0.41	$(1.33 \pm 0.03) \times 10^{30}$	$(5.95 \pm 1.52) \times 10^8$	$(1.72 \pm 0.45) \times 10^{15}$

radially (Zhang et al. 2023). Unfortunately, the outcomes are not acceptable after many trials. Considering that a MFR is a part of a torus (Chen 1989; Titov & Démoulin 1999), we fit the HC with a torus. The parametric equations of a ring torus

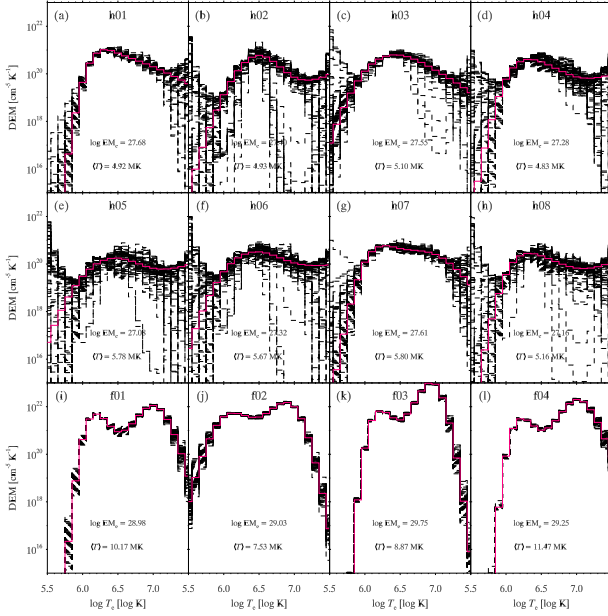


Figure 7. Reconstructed DEM profiles of the eight regions within the HC (a)-(h) and four regions within the flare site (i)-(l). The red solid lines represent the best-fitted DEM curves from the observed values. The black dashed lines represent the DEM curves from 100 MC simulations. The values of $\langle T \rangle$ and $\log EM_c$ are labeled.

(or donut) is:

$$\begin{cases} x(\theta, \phi) = (R + r \cos \theta) \cos \phi + x_0, \\ y(\theta, \phi) = (R + r \sin \theta) \cos \phi + y_0, \\ z(\theta, \phi) = r \sin \phi + z_0, \end{cases} \quad (6)$$

where $0 \leq \theta < 2\pi$, $0 \leq \phi < 2\pi$, R and r stand for the radius of the circular axis and radius of the tube ($r < R$), respectively. The volume of such a torus is $V_{rt} = 2\pi^2 R r^2$.

In this study, the axis of the HC is not circular during eruption, implying that an ellipse would be more suitable. Thereby, the parametric equations of an elliptic torus is:

$$\begin{cases} x(\theta, \phi) = (R_1 + r \cos \theta) \cos \phi + x_0, \\ y(\theta, \phi) = (R_2 + r \sin \theta) \cos \phi + y_0, \\ z(\theta, \phi) = r \sin \phi + z_0, \end{cases} \quad (7)$$

where R_1 and R_2 represent the semi major axes of the ellipse ($R_1 < R_2$). The maximal LOS depth of such a torus is $H = 2r$ and the total volume is $V_{et} = \pi r^2 (2\pi R_1 + 4(R_2 - R_1))$.

In Figure 2(d), the outer and inner boundaries of the HC and flare are delineated with magenta and yellow “+” symbols. Since the footpoints of the HC may blend with the hot PFLs, we fit the HC and PFLs together with an elliptic torus. In Figure 8(a), the same boundaries are delineated with blue and cyan “+” symbols, respectively. The fitted elliptic torus is overlaid with red dots in XY plane, where $R_1 = 108''.4$, $R_2 = 149''.0$, $r = 33''.7$, $x_0 = -1042''.9$, $y_0 = 158''.5$, and $z_0 = 0''$. The shorter section between two green solid lines represents the flare region, while the longer section represents the HC. In Figure 8(b), the elliptic torus is superposed

Table 2. Different energy components of the HC, flare, and CME on 2011 September 22.

Energy	Value (erg)
E_{tHC}	$(1.77 \pm 0.61) \times 10^{30}$
E_{kHC}	$(2.90 \pm 0.79) \times 10^{30}$
E_{HC}	$(4.66 \pm 1.39) \times 10^{30}$
E_{tFL}	$(1.63 \pm 0.04) \times 10^{31}$
E_{rFL}	$(1.03 - 1.31) \times 10^{31}$
E_{nth}	$(5.44 \pm 0.13) \times 10^{31}$
E_{kCME}	$(3.43 \pm 0.94) \times 10^{31}$
E_{pCME}	$(2.66 \pm 0.49) \times 10^{30}$
E_{CME}	$(3.69 \pm 0.98) \times 10^{31}$

on the AIA 131 Å image at 10:36:45 UT with magenta dots. It is obvious that the elliptic torus is in accordance with most of the HC, except for the top part. Figure 8(c) shows 3D visualization of the whole torus with *Matlab*. The total volume of the torus is $V_{et} \approx 1.14 \times 10^{30} \text{ cm}^3$. Considering that the interface between the HC and PFLs is unclear, we pinpoint the interface manually for ten times and calculate the associated volume of HC separately. It is found that the HC occupies 0.80 ± 0.02 of V_{et} , i.e., $(0.91 \pm 0.02) \times 10^{30} \text{ cm}^3$.

Since AR 11302 is very close to the limb, the tilt angle (γ) of the polarity inversion line (PIL) in the photosphere with respect to the longitude line is unknown. As mentioned above, the flare and CME are also captured by the Extreme-UltraViolet Imager (EUVI; Howard et al. 2008) on board STB. Figure 9 shows the full-disk 195 Å image at 11:16:23 UT and 171 Å image at 12:14:53 UT. The orange dashed lines represent the longitude line passing through AR 11302. The short magenta lines represent the PIL, which is parallel to the flare ribbons. Assuming that the HC is along the PIL before eruption, the plane of HC deviates from the plane of sky (POS) by $\gamma \approx 47^\circ$. After correcting the projection effect, the true volume of the HC (V_{HC}) increases by a factor of $f = (\cos \gamma)^{-1} \approx 1.466$ to $(1.33 \pm 0.03) \times 10^{30} \text{ cm}^3$. Meanwhile, the LOS depth increases by a factor of f , resulting in $H = 2rf \approx 71.6 \text{ Mm}$. The average electron number density within the HC is $n_e = \sqrt{EM_c/H} = (5.95 \pm 1.52) \times 10^8 \text{ cm}^{-3}$ when $EM_c \in [1.4, 4.0] \times 10^{27}$. Assuming a filling factor of unity (Kontar et al. 2017), thermal energy of the HC is:

$$E_{tHC} = 3n_e k_B \langle T \rangle V_{HC}, \quad (8)$$

where $k_B = 1.38 \times 10^{-16} \text{ erg K}^{-1}$ is the Boltzmann constant. Using the above values (n_e , $\langle T \rangle$, and V_{HC}) including

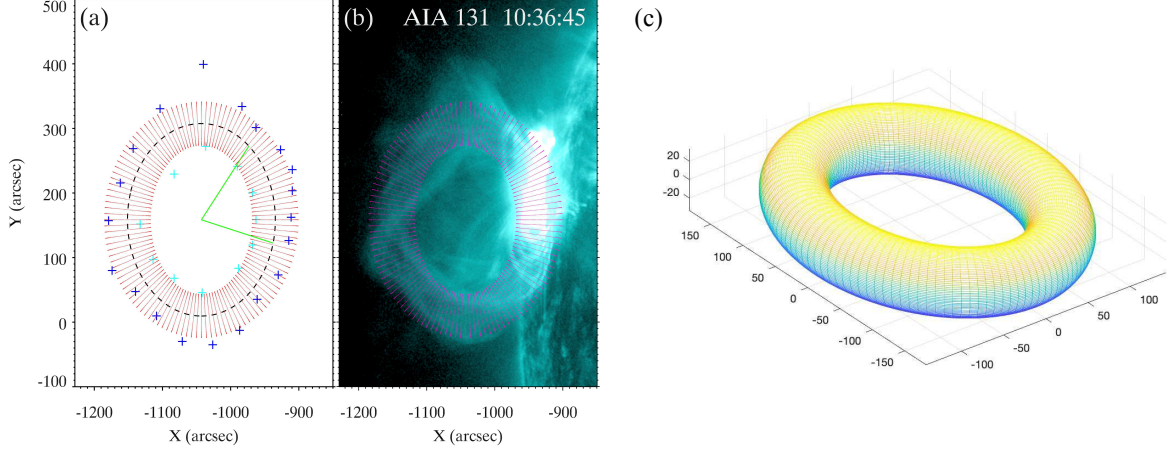


Figure 8. (a) Outer (blue “+” symbols) and inner (cyan “+” symbols) boundaries of the HC. The elliptic torus is superposed with red dots. The black dashed line denotes the elliptic axis. Two green solid lines are used to separate the flare from HC. (b) AIA 131 Å image at 10:36:45 UT superposed by the elliptic torus (magenta dots). (c) 3D visualization of the elliptic torus with *Matlab*.

their uncertainties, three arrays with the same number of elements are created separately. The mean values and standard derivations of these arrays are consistent with the mean values and uncertainties of the physical parameters. The product of these arrays is employed to obtain the average and standard derivation of E_{IHC} , yielding $E_{IHC} = (1.77 \pm 0.61) \times 10^{30}$ erg (Table 2).

Assuming the coronal abundance, the total mass of the HC is $m_{HC} = 1.3m_p n_e V_{HC} \approx (1.72 \pm 0.47) \times 10^{15}$ g, where m_p is the mass of proton. In Figure 4(b), v_{HC} increases to ~ 581 km s $^{-1}$ at 10:36:45 UT. The kinetic energy of the HC is $E_{kHC} = \frac{1}{2}m_{HC}v_{HC}^2 \approx (2.90 \pm 0.79) \times 10^{30}$ erg. The total energy of the HC, including the thermal and kinetic components, reaches $(4.66 \pm 1.39) \times 10^{30}$ erg, which is close to that of the HC on 2010 November 3 (Hannah & Kontar 2013). In Figure 5, as mentioned above, the CME most probably originates from the eruptive HC. Therefore, m_{HC} is considered as a lower limit of the mass of CME (m_{CME}) owing to the mass pileup during its propagation. The velocity of CME ($v_{CME} \approx 1905$ km s $^{-1}$) is derived from linear fitting of the CME height with time. A lower limit of the kinetic energy of the CME is $E_{kCME} = \frac{1}{2}m_{CME}v_{CME}^2 \approx (3.12 \pm 0.85) \times 10^{31}$ erg. Assuming an increment of the CME mass by $\sim 10\%$ during its propagation, m_{CME} reaches $(1.89 \pm 0.52) \times 10^{15}$ g, which is close to the mass of CME front on 2011 September 13 derived by using the WL observation (Ying et al. 2023). In consequence, the kinetic energy of CME increases to $(3.43 \pm 0.94) \times 10^{31}$ erg, which is one order of magnitude larger than that of HC (Table 2).

The potential energy of the CME is (Li et al. 2023):

$$E_{pCME} = GM_{\odot}m_{CME}\left(\frac{1}{R_{\odot}} - \frac{1}{R_{CME}}\right), \quad (9)$$

where G is the gravitational constant, M_{\odot} and R_{\odot} represent the mass and radius of the Sun, R_{CME} denotes the mass cen-

ter of the CME, which increases with time. E_{pCME} falls in the range of $(2.66 \pm 0.49) \times 10^{30}$ erg during its propagation in the FOV of LASCO, which accounts for $\sim 8\%$ of the kinetic energy. The total CME energy, consisting of the kinetic and potential components, is estimated to be $(3.69 \pm 0.98) \times 10^{31}$ erg.

Thermal energy of the flare is (Kontar et al. 2017; Zhang et al. 2019):

$$E_{tFL} = 3k_B T_{FL} \sqrt{EM_V} \times V_{FL} = 3k_B T_{FL} \sqrt{EM_V} A_{FL}^{3/4}, \quad (10)$$

where T_{FL} , A_{FL} , $V_{FL} = A_{FL}^{3/2}$, and EM_V stand for the temperature, area, volume, and volume emission measure of the flare, respectively. Figure 1(b) shows the time evolutions of T_{FL} (orange line) and EM_V (green line) recorded by the GOES spacecraft during 10:20–12:20 UT. The two parameters sequentially reach their maxima at 10:44:13 UT and 11:03:15 UT, while the composite parameter $T_{FL} \sqrt{EM_V}$ reaches maximum at 10:57:08 UT. Figure 2(h) shows SXR image of the flare at 6–12 keV during 10:54–10:58 UT, where A_{FL} is defined as the total area of pixels whose intensities are above $(0.50 \pm 0.01)I_M$. Here, I_M denotes the maximum intensity of the SXR image. After correcting the projection effect by a factor of $f \approx 1.466$, $A_{FL} \approx (1.69 \pm 0.06) \times 10^{19}$ cm 2 and $V_{FL} \approx (6.95 \pm 0.37) \times 10^{28}$ cm 3 . Therefore, the peak thermal energy of the flare is $(1.63 \pm 0.04) \times 10^{31}$ erg.

Figure 1(c) shows variation of the radiative energy loss rate ($L_r(t)$) from SXR-emitting plasma, where background level (L_b) is plotted with an olive dashed line. Hence, the total background-subtracted radiative energy loss is:

$$E_{rFL} = \int (L_r(t) - L_b) dt. \quad (11)$$

The integral during 10:20–12:20 UT results in a value of $\sim 1.31 \times 10^{31}$ erg. An alternative way of estimating E_{rFL} based

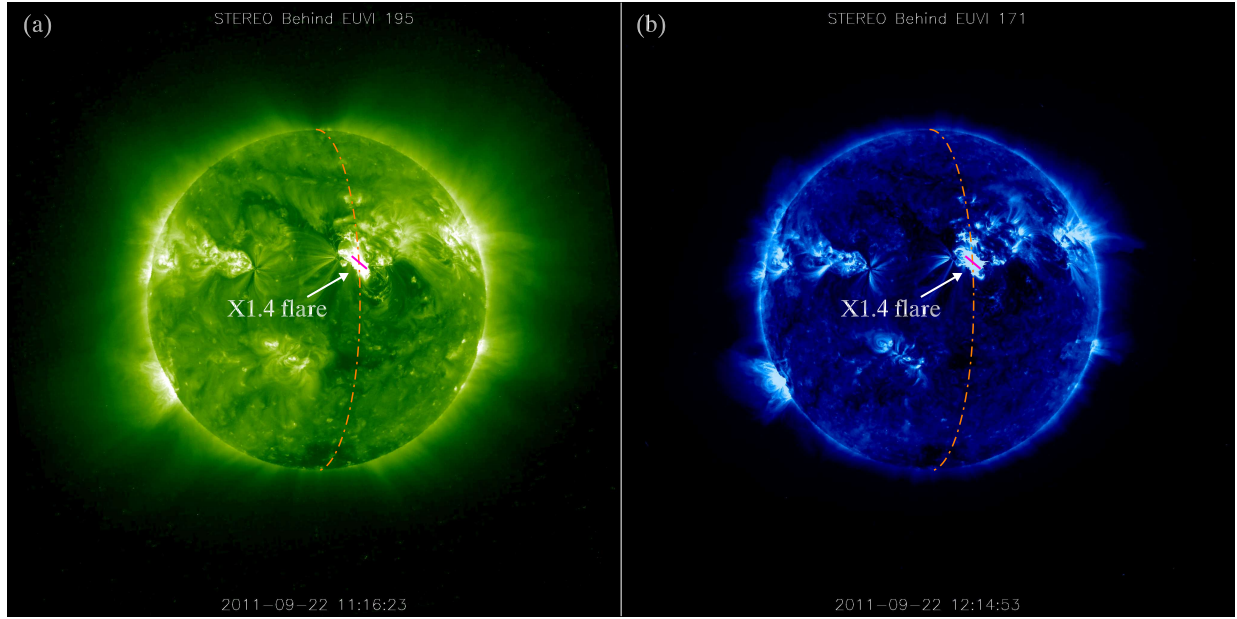


Figure 9. Full-disk STB/EUVI 195 Å image at 11:16:23 UT (a) and 171 Å image at 12:14:53 UT (b). The orange dot-dashed lines represent the longitude line passing through AR 11302. The short magenta lines represent the PIL. The arrows point to PFLs of the X1.4 flare.

on EM_V and $\Lambda(T_{FL})$ is (Zhang et al. 2019):

$$E_{rFL} = \int EM_V(t) \times \Lambda(T_{FL}(t)) dt, \quad (12)$$

where $\Lambda(T_{FL})$ denotes radiative loss rate of the PFLs (Cox & Tucker 1969; Del Zanna et al. 2021). The integral during the same period of time gives rise to a value of $\sim 1.03 \times 10^{31}$ erg. Therefore, E_{rFL} is between 1.03×10^{31} and 1.31×10^{31} erg. All the energy components are listed in Table 2.

4. DISCUSSION

There is a long debate on when a HC is formed. Observational evidences are abundant in favor of formation of a HC before eruption (Cheng et al. 2013a; Zhang et al. 2022b) as well as during eruption (Cheng et al. 2011; Song et al. 2014; Gou et al. 2019; Yan et al. 2021). In our study, the HC is obviously formed before eruption, since the onset time of its fast rise is earlier than the start time of flare in Figure 4 (see also Cheng et al. 2020; Nindos et al. 2020). The HC is visible in 131 Å until $\sim 10:40$ UT before escaping from the FOV of AIA, implying that a lower limit of the HC lifetime in 131 Å is ~ 20 minutes. Considering the high temperature of HCs, the cooling time due to heat conduction is short (Cargill 1994):

$$\tau_{HC} = 4 \times 10^{-10} \frac{n_e L_{HC}^2}{\langle T \rangle^{5/2}}, \quad (13)$$

where n_e , $\langle T \rangle$, and L_{HC} represent the average density, temperature, and half length of a HC, respectively. Using the observed values of $n_e = (5.95 \pm 1.52) \times 10^8 \text{ cm}^{-3}$, $\langle T \rangle \simeq 5.27 \pm 0.41 \text{ MK}$, $L_{HC} \simeq (2.50 \pm 0.06) \times 10^{10} \text{ cm}$, τ_{HC} is

estimated to be 340–4260 s. The cooling time by radiation is estimated to be $\sim 3.0 \times 10^5$ s, which is much longer than τ_{HC} . The short conductive cooling time of a HC suggests that continuous heating is needed to balance the rapid conductive cooling, presumably by magnetic reconnection (Hannah & Kontar 2013). Chen et al. (2019) explored the formation and eruption of a HC on 2014 March 20. It is revealed that heating and buildup of the HC is most probably due to tether-cutting reconnection at the hyperbolic flux tube in the precursor phase. Recently, Cheng et al. (2023) investigated the thermal and kinetic evolutions of a hot MFR, especially the slow-rise precursor phase on 2012 March 13. It is found that moderate magnetic reconnection at the X-shaped high-temperature plasma sheet is important for the formation and heating of pre-eruptive MFR up to ~ 8 MK.

During an eruptive flare associated with a CME, the magnetic free energy is impulsively released and mainly converted into radiation, thermal, and nonthermal energies of the flare, and kinetic, potential energies of the CME (Emslie et al. 2012; Aschwanden et al. 2017). The energy partitions in flares and CMEs are generally in the same order of magnitude (Emslie et al. 2004, 2005; Feng et al. 2013; Li et al. 2023). In this study, the peak thermal energy, total radiative energy loss of the flare, and kinetic energy of the CME are in the same order of magnitude ($\sim 10^{31}$ erg). It should be emphasized that the bulk kinetic energy of turbulent motions at the flare loop top (Kontar et al. 2017) as well as the prompt component of solar energetic particles (Li et al. 2023) are not taken into account because they contribute only negligible fractions. Owing to the lack of data from RHESSI before 10:54 UT, we are unable to calculate nonthermal en-

ergy of the flare-accelerated electrons (E_{nth}). However, statistical investigation reveals that an excellent correlation exists between the peak thermal energy and nonthermal energy. The ratio between the two components has a median value of 0.3 ± 0.02 (Warmuth & Mann 2016). Hence, E_{nth} is in the range of $(5.44 \pm 0.13) \times 10^{31}$ erg, which is sufficient to heat and sustain SXR-emitting plasma in the flare (Zhang et al. 2019).

In Table 2, the thermal and kinetic energies of the HC are a few 10^{30} erg, which are one order of magnitude lower than the flare energies. Nevertheless, the ratio $\frac{E_{HC}}{E_{FL}} \approx 0.11 \pm 0.03$ is significant, indicating that thermal energy of the HC should be taken into account in energy partition. The magnetic free energy, which is predominantly stored in a MFR before flare, is estimated to be $\sim 10^{32}$ erg for a normal X-class flare (Guo et al. 2008). Assuming the magnetic field strength (B) and volume of the HC are ~ 150 G (Guo et al. 2021) and $(1.33 \pm 0.03) \times 10^{29}$ cm³ before eruption, the total magnetic energy is estimated to be $E_{mag} = \frac{B^2}{8\pi} V_{HC} \approx (1.20 \pm 0.03) \times 10^{32}$ erg. It is obvious that most of the magnetic free energy is released and distributed into the flare and CME, only a few percent is used to heat the HC. Intermittent magnetic reconnections in the flare current sheet may play a role in sustaining the hot temperature of the HC. MHD numerical simulations are especially desired to figure out the formation and thermal evolution of HCs (Cheng et al. 2023). The elliptic torus shape of HCs (Figure 8) inspired by theoretical MFR models (Chen 1989; Titov & Démoulin 1999) is highly beneficial to the calculations of volume, mass, thermal energy, and kinetic energy in statistical analysis. Multi-point observations of HCs in EUV and SXR passbands, especially from the Sun-Earth Lagrange point L5, are expected in next-generation solar telescopes (Liu et al. 2010b; Gopalswamy et al. 2023) to facilitate 3D reconstructions of HCs.

It should be emphasized that the HC is visible in AIA 131 and 94 Å images until $\sim 10:39$ UT. The thermal energy of the X1.4 flare reaches its maximum at $\sim 10:57$ UT. The CME is visible in the FOV of LASCO during 10:48–11:12 UT. The total radiative loss of SXR-emitting plasma is an integral during 10:20–12:20 UT. Accordingly, it is difficult to compare the energy components at the same instant (Emslie et al. 2004, 2005, 2012; Feng et al. 2013; Aschwanden et al. 2017; Li et al. 2023). Moreover, as the HC rises and expands, the shape is only regular (resembling an elliptic torus) during 10:35:09–10:37:33 UT, when elliptic torus fitting is applicable to the volume estimation. This is an limitation of the present work. So, there is no need to investigate the temporal evolution of the thermal and kinetic energies of the HC. In the future, we will find more cases to study the evolutions in a statistical way.

5. CONCLUSION

In this paper, we carry out multiwavelength and multiview observations of the eruption of a HC, which generates an X1.4 flare and a fast CME on 2011 September 22. We focus on the energetics of the HC and compare with energy components of the related flare and CME. The main results are as follows:

1. The thermal and kinetic energies of the HC are $(1.77 \pm 0.61) \times 10^{30}$ erg and $(2.90 \pm 0.79) \times 10^{30}$ erg, respectively. The peak thermal energy of the flare and total radiative loss of SXR-emitting plasma are $(1.63 \pm 0.04) \times 10^{31}$ erg and $(1.03 - 1.31) \times 10^{31}$ erg, respectively. The ratio between the thermal energies of HC and flare is 0.11 ± 0.03 , suggesting that thermal energy of the HC is not negligible. The kinetic and potential energies of the CME are $(3.43 \pm 0.94) \times 10^{31}$ erg and $(2.66 \pm 0.49) \times 10^{30}$ erg, giving rise to a total energy of $(3.69 \pm 0.98) \times 10^{31}$ erg for the CME.
2. Continuous heating of the HC is required to balance the rapid cooling by heat conduction, which probably originate from intermittent magnetic reconnection at the flare current sheet. Our investigation will shed light on the accumulation, release, and conversion of energies in large-scale solar eruptions.

The authors appreciate the referee for valuable suggestions to improve the quality of this article. We also thank Drs. Yuandeng Shen, Lei Ni, Zhike Xue, and Xiaoli Yan for inspiring discussions. SDO is a mission of NASA's Living With a Star Program. AIA data are courtesy of the NASA/SDO science teams. STEREO/SECCHI data are provided by a consortium of US, UK, Germany, Belgium, and France. The e-Callisto data are courtesy of the Institute for Data Science FHNW Brugg/Windisch, Switzerland. This work is supported by the Strategic Priority Research Program of the Chinese Academy of Sciences, Grant No. XDB0560000, the National Key R&D Program of China 2022YFF0503003 (2022YFF0503000), NSFC under the grant numbers 12373065, 12325303, 12073081, and Yunnan Key Laboratory of Solar Physics and Space Science under the grant number YNSPCC202206. J.D. is supported by the Special Research Assistant Project CAS.

REFERENCES

- Amari, T., Luciani, J. F., Aly, J. J., et al. 2003, ApJ, 585, 1073. doi:10.1086/345501
- Aschwanden, M. J., Caspi, A., Cohen, C. M. S., et al. 2017, ApJ, 836, 17. doi:10.3847/1538-4357/836/1/17

- Aulanier, G. & Dudík, J. 2019, *A&A*, 621, A72.
doi:10.1051/0004-6361/201834221
- Aulanier, G., Török, T., Démoulin, P., et al. 2010, *ApJ*, 708, 314.
doi:10.1088/0004-637X/708/1/314
- Awasthi, A. K., Liu, R., Wang, H., et al. 2018, *ApJ*, 857, 124.
doi:10.3847/1538-4357/aab7fb
- Bain, H. M., Krucker, S., Saint-Hilaire, P., et al. 2014, *ApJ*, 782, 43. doi:10.1088/0004-637X/782/1/43
- Brueckner, G. E., Howard, R. A., Koomen, M. J., et al. 1995, *SoPh*, 162, 357. doi:10.1007/BF00733434
- Cargill, P. J. 1994, *ApJ*, 422, 381. doi:10.1086/173733
- Chen, J. 1989, *ApJ*, 338, 453. doi:10.1086/167211
- Chen, P. F. 2011, *Living Reviews in Solar Physics*, 8, 1.
doi:10.12942/lrsp-2011-1
- Chen, P. F. & Shibata, K. 2000, *ApJ*, 545, 524. doi:10.1086/317803
- Chen, H., Yang, J., Ji, K., et al. 2019, *ApJ*, 887, 118.
doi:10.3847/1538-4357/ab527e
- Cheng, X., Zhang, J., Liu, Y., et al. 2011, *ApJL*, 732, L25.
doi:10.1088/2041-8205/732/2/L25
- Cheng, X., Zhang, J., Saar, S. H., et al. 2012, *ApJ*, 761, 62.
doi:10.1088/0004-637X/761/1/62
- Cheng, X., Zhang, J., Ding, M. D., et al. 2013a, *ApJ*, 763, 43.
doi:10.1088/0004-637X/763/1/43
- Cheng, X., Zhang, J., Ding, M. D., et al. 2013b, *ApJL*, 769, L25.
doi:10.1088/2041-8205/769/2/L25
- Cheng, X., Ding, M. D., Zhang, J., et al. 2014, *ApJL*, 789, L35.
doi:10.1088/2041-8205/789/2/L35
- Cheng, X., Ding, M. D., & Fang, C. 2015, *ApJ*, 804, 82.
doi:10.1088/0004-637X/804/2/82
- Cheng, X., Guo, Y., & Ding, M. 2017, *Science China Earth Sciences*, 60, 1383. doi:10.1007/s11430-017-9074-6
- Cheng, X., Zhang, J., Kliem, B., et al. 2020, *ApJ*, 894, 85.
doi:10.3847/1538-4357/ab886a
- Cheng, X., Xing, C., Aulanier, G., et al. 2023, *ApJL*, 954, L47.
doi:10.3847/2041-8213/acf3e4
- Cox, D. P. & Tucker, W. H. 1969, *ApJ*, 157, 1157.
doi:10.1086/150144
- Del Zanna, G., Dere, K. P., Young, P. R., et al. 2021, *ApJ*, 909, 38.
doi:10.3847/1538-4357/abd8ce
- Dere, K. P., Brueckner, G. E., Howard, R. A., et al. 1999, *ApJ*, 516, 465. doi:10.1086/307101
- Emslie, A. G., Kucharek, H., Dennis, B. R., et al. 2004, *Journal of Geophysical Research (Space Physics)*, 109, A10104.
doi:10.1029/2004JA010571
- Emslie, A. G., Dennis, B. R., Holman, G. D., et al. 2005, *Journal of Geophysical Research (Space Physics)*, 110, A11103.
doi:10.1029/2005JA011305
- Emslie, A. G., Dennis, B. R., Shih, A. Y., et al. 2012, *ApJ*, 759, 71.
doi:10.1088/0004-637X/759/1/71
- Feng, L., Wiegmann, T., Su, Y., et al. 2013, *ApJ*, 765, 37.
doi:10.1088/0004-637X/765/1/37
- Green, L. M., Kliem, B., & Wallace, A. J. 2011, *A&A*, 526, A2.
doi:10.1051/0004-6361/201015146
- Gopalswamy, N., Christe, S., Fung, S., et al. 2023, *BAAS*.
doi:10.3847/25c2cfcb.0c98a944
- Gou, T., Liu, R., Kliem, B., et al. 2019, *Science Advances*, 5, 7004.
doi:10.1126/sciadv.aau7004
- Guo, Y., Ding, M. D., Wiegmann, T., et al. 2008, *ApJ*, 679, 1629.
doi:10.1086/587684
- Guo, Y., Zhong, Z., Ding, M. D., et al. 2021, *ApJ*, 919, 39.
doi:10.3847/1538-4357/ac10c8
- Hannah, I. G. & Kontar, E. P. 2012, *A&A*, 539, A146.
doi:10.1051/0004-6361/201117576
- Hannah, I. G. & Kontar, E. P. 2013, *A&A*, 553, A10.
doi:10.1051/0004-6361/201219727
- Hou, Y. J., Zhang, J., Li, T., et al. 2018, *A&A*, 619, A100.
doi:10.1051/0004-6361/201732530
- Howard, R. A., Moses, J. D., Vourlidas, A., et al. 2008, *SSRv*, 136, 67. doi:10.1007/s11214-008-9341-4
- Hurford, G. J., Schmahl, E. J., Schwartz, R. A., et al. 2002, *SoPh*, 210, 61. doi:10.1023/A:1022436213688
- James, A. W., Green, L. M., Palmerio, E., et al. 2017, *SoPh*, 292, 71. doi:10.1007/s11207-017-1093-4
- Jenkins, J. M. & Keppens, R. 2021, *A&A*, 646, A134.
doi:10.1051/0004-6361/202039630
- Jiang, C., Feng, X., Liu, R., et al. 2021, *Nature Astronomy*, 5, 1126. doi:10.1038/s41550-021-01414-z
- Joshi, N. C., Liu, C., Sun, X., et al. 2015, *ApJ*, 812, 50.
doi:10.1088/0004-637X/812/1/50
- Kaiser, M. L., Kucera, T. A., Davila, J. M., et al. 2008, *SSRv*, 136, 5. doi:10.1007/s11214-007-9277-0
- Karlický, M. 2023, arXiv:2307.07144.
doi:10.48550/arXiv.2307.07144
- Kliem, B., Karlický, M., & Benz, A. O. 2000, *A&A*, 360, 715.
doi:10.48550/arXiv.astro-ph/0006324
- Kou, Y., Cheng, X., Wang, Y., et al. 2022, *Nature Communications*, 13, 7680. doi:10.1038/s41467-022-35377-0
- Kontar, E. P., Perez, J. E., Harra, L. K., et al. 2017, *PhRvL*, 118, 155101. doi:10.1103/PhysRevLett.118.155101
- Lemen, J. R., Title, A. M., Akin, D. J., et al. 2012, *SoPh*, 275, 17.
doi:10.1007/s11207-011-9776-8
- Li, D., Warmuth, A., Wang, J., et al. 2023, *Research in Astronomy and Astrophysics*, 23, 095017. doi: 10.1088/1674-4527/acd592
- Liakh, V. & Keppens, R. 2023, *ApJL*, 953, L13.
doi:10.3847/2041-8213/acea78
- Lin, J. & Forbes, T. G. 2000, *J. Geophys. Res.*, 105, 2375.
doi:10.1029/1999JA900477
- Lin, R. P., Dennis, B. R., Hurford, G. J., et al. 2002, *SoPh*, 210, 3.
doi:10.1023/A:1022428818870

- Liu, R. 2020, *Research in Astronomy and Astrophysics*, 20, 165.
doi:10.1088/1674-4527/20/10/165
- Liu, R., Liu, C., Wang, S., et al. 2010, *ApJL*, 725, L84.
doi:10.1088/2041-8205/725/1/L84
- Liu, Y., Thernisien, A., Luhmann, J. G., et al. 2010, *ApJ*, 722, 1762. doi:10.1088/0004-637X/722/2/1762
- Liu, Y., Su, Y., Liu, R., et al. 2022, *ApJ*, 941, 83.
doi:10.3847/1538-4357/aca08c
- Lynch, B. J., Antiochos, S. K., MacNeice, P. J., et al. 2004, *ApJ*, 617, 589. doi:10.1086/424564
- Moore, R. L., Sterling, A. C., Hudson, H. S., et al. 2001, *ApJ*, 552, 833. doi:10.1086/320559
- Nindos, A., Patsourakos, S., Vourlidas, A., et al. 2015, *ApJ*, 808, 117. doi:10.1088/0004-637X/808/2/117
- Nindos, A., Patsourakos, S., Vourlidas, A., et al. 2020, *A&A*, 642, A109. doi:10.1051/0004-6361/202038832
- Okamoto, T. J., Tsuneta, S., Lites, B. W., et al. 2008, *ApJL*, 673, L215. doi:10.1086/528792
- Rust, D. M. & Kumar, A. 1996, *ApJL*, 464, L199.
doi:10.1086/310118
- Savcheva, A., Pariat, E., van Ballegoijen, A., et al. 2012, *ApJ*, 750, 15. doi:10.1088/0004-637X/750/1/15
- Savcheva, A., Pariat, E., McKillop, S., et al. 2016, *ApJ*, 817, 43.
doi:10.3847/0004-637X/817/1/43
- Song, H. Q., Zhang, J., Chen, Y., et al. 2014, *ApJL*, 792, L40.
doi:10.1088/2041-8205/792/2/L40
- Song, H., Zhang, J., Li, L., et al. 2023a, *ApJ*, 942, 19.
doi:10.3847/1538-4357/aca6e0
- Song, H., Li, L., Zhou, Z., et al. 2023b, *ApJL*, 952, L22.
doi:10.3847/2041-8213/ace422
- Titov, V. S. & Démoulin, P. 1999, *A&A*, 351, 707
- Török, T. & Kliem, B. 2005, *ApJL*, 630, L97. doi:10.1086/462412
- van Ballegoijen, A. A. & Martens, P. C. H. 1989, *ApJ*, 343, 971.
doi:10.1086/167766
- Vasanth, V., Chen, Y., Lv, M., et al. 2019, *ApJ*, 870, 30.
doi:10.3847/1538-4357/aaeffd
- Vemareddy, P., Démoulin, P., Sasikumar Raja, K., et al. 2022, *ApJ*, 927, 108. doi:10.3847/1538-4357/ac4dfe
- Vourlidas, A., Lynch, B. J., Howard, R. A., et al. 2013, *SoPh*, 284, 179. doi:10.1007/s11207-012-0084-8
- Wang, Y., Su, Y., Shen, J., et al. 2018, *ApJ*, 859, 148.
doi:10.3847/1538-4357/aac0f7
- Warmuth, A. & Mann, G. 2016, *A&A*, 588, A116.
doi:10.1051/0004-6361/201527475
- Wu, Z., Chen, Y., Huang, G., et al. 2016, *ApJL*, 820, L29.
doi:10.3847/2041-8205/820/2/L29
- Xia, C., Keppens, R., & Guo, Y. 2014, *ApJ*, 780, 130.
doi:10.1088/0004-637X/780/2/130
- Xing, C., Cheng, X., & Ding, M. D. 2020, *The Innovation*, 1, 100059. doi:10.1016/j.xinn.2020.100059
- Xue, Z., Yan, X., Cheng, X., et al. 2016, *Nature Communications*, 7, 11837. doi:10.1038/ncomms11837
- Xue, Z., Yan, X., Yang, L., et al. 2017, *ApJL*, 840, L23.
doi:10.3847/2041-8213/aa7066
- Yan, X. L., Yang, L. H., Xue, Z. K., et al. 2018, *ApJL*, 853, L18.
doi:10.3847/2041-8213/aaa6c2
- Yan, X., Wang, J., Guo, Q., et al. 2021, *ApJ*, 919, 34.
doi:10.3847/1538-4357/ac116d
- Ying, B., Bemporad, A., Feng, L., et al. 2023, *ApJ*, 942, 3.
doi:10.3847/1538-4357/aca52c
- Zhang, Q. M. & Ji, H. S. 2014, *A&A*, 567, A11.
doi:10.1051/0004-6361/201423698
- Zhang, J., Cheng, X., & Ding, M.-D. 2012, *Nature Communications*, 3, 747. doi:10.1038/ncomms1753
- Zhang, Q. M., Ji, H. S., & Su, Y. N. 2016, *SoPh*, 291, 859.
doi:10.1007/s11207-016-0878-1
- Zhang, Q. M., Cheng, J. X., Feng, L., et al. 2019, *ApJ*, 883, 124.
doi:10.3847/1538-4357/ab3a52
- Zhang, Q. M., Chen, J. L., Li, S. T., et al. 2022a, *SoPh*, 297, 18.
doi:10.1007/s11207-022-01952-3
- Zhang, Q., Li, C., Li, D., et al. 2022b, *ApJL*, 937, L21.
doi:10.3847/2041-8213/ac8e01
- Zhang, Q.-M., Hou, Z.-Y., & Bai, X.-Y. 2023, arXiv:2307.00943.
doi:10.48550/arXiv.2307.00943
- Zhou, Y.-H., Xia, C., Keppens, R., et al. 2018, *ApJ*, 856, 179.
doi:10.3847/1538-4357/aab614
- Zhou, Y., Ji, H., & Zhang, Q. 2023, *SoPh*, 298, 35.
doi:10.1007/s11207-023-02126-5
- Zucca, P., Carley, E. P., Bloomfield, D. S., et al. 2014, *A&A*, 564, A47. doi:10.1051/0004-6361/201322650